DeepGEM-EGF: A Bayesian strategy for joint estimates of source-time functions and empirical Green's functions

Théa Ragon[1,2], Angela F. Gao[3], Zachary E. Ross[1]

[1]Seismological Laboratory, California Institute of Technology, Pasadena, CA, USA.
[2]*now at* CNRS, Univ. Grenoble Alpes, IRD, ISTerre, Grenoble, France
[3]Computing and Mathematical Sciences Department, California Institute of Technology, Pasadena, CA, USA

Key Points:

- We propose a new Bayesian framework for estimating source time functions and optimizing one or several prior Empirical Green's Functions (EGFs)
- DeepGEM-EGF accounts for epistemic uncertainties and efficiently discriminates source parameters given approximations made in the forward model
- DeepGEM-EGF robustly estimates complex source time functions with high-frequency content and exhibits limited sensitivity to prior EGF(s) selection

Corresponding author: Théa Ragon, `thea.ragon@univ-grenoble-alpes.fr`

Abstract

An earthquake record is the convolution of source radiation, path propagation and site effects, and instrument response. Isolating the source component requires solving an ill-posed inverse problem. Whether the instability of inferred source parameters arises from varying properties of the source, or from approximations we introduce in solving the problem, remains an open question. Such approximations often derive from limited knowledge of the forward problem. The Empirical Green's function (EGF) approach offers a partial remedy by approximating the forward response of larger events using the records of small events. Indeed, the choice of the « best » small event drastically influences the properties estimated for the larger earthquake. Discriminating variability in source properties from epistemic uncertainties, stemming from the forward problem or other modeling assumptions, requires us to reliably account for, and propagate, any bias or trade-off introduced in the problem. We propose a Bayesian inversion framework that aims at providing reliable and probabilistic estimates of source parameters (here, for the source-time function or STF), and their posterior uncertainty, in the time domain. We jointly solve for the best EGF using one or a few small events as *prior* EGF. Our approach is based on DeepGEM, an unsupervised generalized expectation-maximization framework for blind inversion (Gao et al., 2021). We demonstrate, with toy models as well as an application to an earthquake swarm in California, the potential of DeepGEM-EGF to disentangle the variability of the seismic source from biases introduced by modeling assumptions.

Plain Language Summary

Our understanding of earthquakes is based on the analysis of earthquakes waveforms recorded at the surface. This non-trivial analysis consists in discriminating properties of the earthquake itself from the footprints of the medium the waves propagate through. In turn, it remains unclear whether the instability of estimated earthquake parameters is inherent to the earthquake nature, or derives from the approximations used in our analysis. The empirical Green's function (EGF) approach offers a partial remedy, in using a small earthquake as a proxy for the propagation term of a larger event. However, the choice of the "best" small event significantly impacts parameters estimated for the larger earthquake. We introduce a probabilistic unsupervised machine learning framework that estimates earthquake source parameters in the time domain (source time functions), and related uncertainties, while discarding the need to select one "best" small event. The approach sequentially updates the properties of an *a priori* selected set of small events towards an optimal solution. We demonstrate the potential of the framework using both simplified models and a case study of an earthquake swarm in California. Our method proves efficient at disentangling earthquake source properties from uncertainties in the modeling process.

1 Introduction

Our understanding of how earthquakes start, grow, and stop resides in our ability to build physical models from observed source and rupture properties. Variations in rupture pattern, velocity and directivity, radiated energy and stress drop are examined to provide constraints on fault zone processes (e.g., Kanamori & Brodsky, 2004). The variability of source parameters has practical implications for hazard assessment as it impacts ground shaking predictions (e.g., Anderson & Brune, 1999; Pavic et al., 2000; Boore, 2003; Cotton et al., 2013; A. S. Baltay et al., 2013; Oth et al., 2017; Gerstenberger et al., 2020). Source (and slip) scaling currently dictates how we relate observations, physical processes and hazard (e.g., Aki, 1996; Cotton et al., 2013; Cocco et al., 2016; Lambert et al., 2021). Yet, our insight on whether large and small earthquakes strictly share similar properties (Aki, 1967), or if their physics diverge, remains nuanced because of the puzzling instability of the source parameters we infer (e.g., Shearer et al., 2006; Viesca & Garagash, 2015; Lin & Lapusta, 2018; Hardebeck, 2020; Abercrombie, 2021; Bindi et al., 2023).

An earthquake record is the convolution of source radiation, path propagation and site effects, and instrument response. Isolating the source component requires solving an ill-posed inverse problem; however there are questions regarding whether such instabilities arise from the source, or from approximations we introduce in the problem. Since the pioneering work of Hartzell (1978), the Empirical Green's function (EGF) approach is a widely used assumption that spares us the need to model a costly forward problem (e.g., Frankel & Kanamori, 1983; Mueller, 1985; Frankel et al., 1986; Hutchings & Wu, 1990; Dreger, 1994; Ihmlé, 1996; Courboulex et al., 1996; Hough, 1997a). Assuming that the only difference in the recordings of two similar and co-located earthquakes is due to their respective rupture, then an event small enough to have an impulsive source can be used as a Green's function for a larger one. However, the choice of the "best" EGF remains a large source of epistemic uncertainties, because of discrepancies in focal mechanism, non-impulsivity of the small event, relative hypocentral distance, finite bandwidth, and noise (e.g., Viegas et al., 2010; Kane et al., 2011, 2013; Abercrombie, 2015, and references therein). Using several potential events (e.g., Hough, 1997b; Abercrombie et al., 2017) or averaging over a dense cluster of events and stations (generalized spectral decomposition, e.g., Andrews, 1986; Prieto et al., 2006; Shearer et al., 2006; Bindi et al., 2009; Trugman & Shearer, 2017) are good palliative approaches, but they fail at accounting for the actual impact of approximations in the forward problem on our understanding of source physics.

Approximations we introduce in the blind source deconvolution problem also derive from data errors, non-physically justified priors and any modeling assumptions. Discriminating variability in source properties from such epistemic uncertainties requires us to reliably account for, and propagate, any uncertainty and trade-off (as already suggested by many authors, e.g., Abercrombie & Rice, 2005; Prieto et al., 2006; Shearer et al., 2019; Trugman, 2022). To do so, spectral ratio analyses have seen recent progress towards Bayesian inversion frameworks, facilitated by the few number of parameters involved (e.g., Godano et al., 2015; Garcia-Aristizabal et al., 2016; Van Houtte & Denolle, 2018; Supino et al., 2019; Törnman et al., 2021; Trugman, 2022). Frequency-domain analyses are usually more popular, for computational speed and the reduced number of parameters. But, whether they be generalized decompositions or spectral divisions, those analyses often require non physically justified regularization (Bertero et al., 1997) or assumptions (e.g., Andrews, 1986; Trugman, 2022), and can be biased by artifacts produced in the time domain (Zollo et al., 1995). By contrast, time-domain analyses could reduce the posterior variability of inferred source parameters (Courboulex et al., 2016) while improving constraints on a few properties such as directivity (Boatwright, 1984; McGuire, 2004; Trugman, 2022). Yet, time-domain analyses are, so far, limited to deterministic optimization approaches (e.g., Vallée, 2004; Plourde & Bostock, 2017; Gallegos & Xie, 2020) that hinder our ability to monitor and assess epistemic variability of the source.

Here, we propose a time-domain Bayesian inversion framework that aims to provide reliable and probabilistic estimates of source parameters and their uncertainty. To do so, we consider the EGF assumption as a potential cause of epistemic uncertainties and discard any oversimplification of the problem. We apply our method on toy models and an application to a swarm in California to demonstrate the potential of this unsupervised approach to deepen our understanding of the source of earthquakes, and in particular of its variability.

2 DeepGEM-EGF: Generalized Expectation-Maximization for blind deconvolution

The approach we propose, DeepGEM-EGF, is twofold: we explore the solution space for any probable source-time function (STF) using one or more candidate EGFs, while considering these EGFs to be a good–but slightly incorrect–prior that needs updating.

The inverse problem that we are trying to solve can be written as $\mathbf{d} = G_\theta(\mathbf{m})$; $\mathbf{d}$ being the observed data, $\mathbf{m}$ the parameters of the inverse problem (the STF), G the forward problem (i.e. convolution with the EGFs), and θ the parameters of G representing the EGFs. Solving for both $\mathbf{m}$ and θ is an ill-posed problem. We want to estimate the posterior uncertainty on the STF, but generally already have good prior knowledge on the forward problem as we have selected one or multiple EGFs. We therefore choose to estimate the posterior probability $p(\mathbf{m}|\mathbf{d}, \theta)$ on $\mathbf{m}$ while solving for one best estimate of θ that maximizes the log likelihood $p(\theta|\mathbf{d})$ considering all of the potential solutions for $\mathbf{m}$.

To do so, we follow an approach derived from DeepGEM (Gao et al., 2021), a variational Bayesian Expectation-Maximization (EM) framework that can be used to solve for the parameters of both an inverse problem and a forward model in an unsupervised manner. DeepGEM was initially designed for blind tomography, but has also proven to be effective for a simple blind image deconvolution problem (Gao et al., 2021). Our EM-like approach iterates between two steps; (1) an E-step that learns an approximation to the posterior distribution of $\mathbf{m}$ given the fixed forward model parameters $\theta^{(i-1)}$ inferred at the previous iteration $i-1$; and (2) an M-step that solves for $\theta^{(i)}$ considering the fixed parameters of the inverse problem solved in the prior E-step. We present here the main characteristics, and modifications from the initial framework, of DeepGEM-EGF.

2.1 Expectation step: solving for the Source-Time Function

The expectation step (i.e E-step) aims to approximate the posterior distribution of our target STF $\mathbf{m}$ knowing the data $\mathbf{d}$ using a normalizing flow-based generative model based on Deep Probabilistic Imaging (DPI, Sun & Bouman, 2021; Sun et al., 2022). We infer the posterior distribution $q_\phi(\mathbf{m})$ using variational inference where the class of normalizing flow-based neural networks defines our variational distribution. Once we have solved for the approximate posterior distribution, $q_\phi(\mathbf{m})$, we can sample from it to solve the M-step.

We parameterize $q_\phi(\mathbf{m})$ with a normalizing flow F_ϕ such that $q_\phi(\mathbf{m}) = p(F_\phi(z))$. F_ϕ allows us to map a complicated distribution $p(F_\phi(z))$ as a composition of L invertible transformations $F_{\phi_L} \circ F_{\phi_{L-1}} \circ ... \circ F_{\phi_1}$ applied to Gaussian samples z where L is the number of layers for the generative flow. At the i-th E-step, we optimize the weights $\phi^{(i)}$ of our $F_{\phi^{(i)}}$ that best approximates our posterior distribution $p(\mathbf{m}|\mathbf{d}, \theta^{(i-1)})$ through the following objective:

$$\begin{aligned}\phi^{(i)} &= \arg\min_\phi \mathrm{KL}\left(q_\phi(\mathbf{m}) \parallel p(\mathbf{m}|\mathbf{d}, \theta^{(i-1)})\right) \\ &\approx \arg\min_\phi \frac{1}{N}\sum_{n=1}^{N}\left[-\log p(\mathbf{d} \mid \theta^{(i-1)}, \mathbf{m}_n) - \log p\left(\mathbf{m}_n\right) + \beta \log q_\phi\left(\mathbf{m}_n\right)\right],\end{aligned} \tag{1}$$

for $\mathbf{m}_n = F_\phi\left(z_n\right)$, $z_n \sim \mathcal{N}(0, 1)$, a batch size of N, the prior on the STF $\log p(\mathbf{m})$, the data likelihood $\log p(\mathbf{d}|\mathbf{m}, \theta^{i-1})$, and KL denotes the Kullback-Leibler divergence. Note that the approximation comes from evaluation of an expectation using Monte Carlo sampling. See full derivations in Sun and Bouman (2021) and Gao et al. (2021). An additional hyperparameter β is proposed in DPI to control the entropy of the generative model's posterior samples. We use a Real-NVP network (Dinh et al., 2016) for F_ϕ with L=32 affine coupling layers. We use Adam (Kingma & Ba, 2014) as the optimizer with a batch size of 1024.

We define a realistic prior over the normalized amplitude of the STF as $p(\mathbf{m}) \sim \mathcal{N}(\overline{\mathbf{m}}, \sigma_m)$. By default, $\overline{\mathbf{m}}$ is a Gaussian-shaped STF and σ_m is of 0.2 sec. The default Gaussian-shaped $\overline{\mathbf{m}}$ is centered on half of the preset STF length, and has a width equal to 10% of the total preset STF duration. We also augment $p(\mathbf{m})$ with a few specific constraints. We want the STF to be close to zero on its boundaries, and we enforce sparsity with a ℓ_1 norm. With sparsity regularization, we avoid overestimating the complexity of the STF due to noise and data over-fitting, while allowing for sharp changes in the solution. We also impose a total variation regularization. Default hyperparameters (weights for the specific constraints) were empirically chosen by inspecting the loss and the fit to synthetic tests on a grid search.

2.2 Maximization step: optimizing the EGFs for the forward model

The maximization step (i.e. M-step) relies on estimates of the approximate posterior $q_\phi(\mathbf{m})$ from the preceding E-step to update θ, the parameters of the unknown forward model, from the initially assumed set of EGF(s). We define G_θ as the convolution between model parameters $\mathbf{m}$ and a linear kernel k_θ of parameters θ. The kernel is a deep network consisting in multiple convolution layers without non-linear activation, as proposed in Bell-Kligler et al. (2019) and successfully applied in Gao et al. (2021):

$$G_\theta(\mathbf{m}) = \mathbf{m} * k_\theta = \mathbf{m} * \frac{\theta_1 * \theta_2 * \ldots * \theta_K}{||\theta_1 * \theta_2 * \ldots * \theta_K||_\infty}, \tag{2}$$

for a K-layer network. During the i-th M-step, we optimize the weights $\theta^{(i)}$ to find the *maximum a posteriori* (MAP) of the posterior distribution of parameters θ knowing the data $\mathbf{d}$:

$$\begin{aligned} \theta^{(i)} &= \arg\max_\theta \log p(\theta \mid \mathbf{d}) \\ &\approx \arg\max_\theta \left[\frac{1}{N} \sum_{n=1}^{N} \left[\log p\left(\mathbf{d} \mid \theta, \mathbf{m}_n\right)\right] + \log p(\theta) \right], \end{aligned} \tag{3}$$

for $\mathbf{m}_n = F_{\phi^{(i)}}(\mathbf{z}_n)$, $\mathbf{z}_n \sim \mathcal{N}(0,1)$. We use K=7 convolution layers to parameterize G_θ. We use Adam as the optimizer.

As we already have a good guess for our forward model, we use a prior $\log p(\theta)$ that encourages the forward model to stay close to the initially assumed set of EGF(s). We define $\log p(\theta)$ as a weighted sum of mean absolute error ($\mathcal{L}_\phi$), ℓ_2-norm, and dynamic time warping norm ($\mathcal{L}_{DTW}$) between the updated and initial EGF(s) k_{θ_0}:

$$\log p(\theta) = \lambda_\phi \overbrace{\sum |k_{\theta_0} - k_{\theta^{(i)}}|}^{\mathcal{L}_\phi} + \lambda_2 \overbrace{\sum (k_{\theta_0} - k_{\theta^{(i)}})^2}^{\ell_2} + \lambda_{DTW} \overbrace{DTW_{0.1}(k_{\theta^{(i)}}, k_{\theta_0})}^{\mathcal{L}_{DTW}}. \tag{4}$$

When considering multiple candidate EGFs, we parameterize k_θ as an array of independent deep networks. During the i-th M-step and for each EGF e, weights $\theta_e^{(i)}$ are optimized. We augment $\log p(\theta)$ with a prior $\mathcal{L}_{\text{multi}}$ that encourages the inferred EGFs to converge towards a single EGF $k_{\theta_{\text{best}}^{(i)}}$ that minimizes $\alpha_e^{(i)}$, the misfit between data and predictions:

$$\log p(\theta) = \mathcal{L}_\phi + \ell_2 + \mathcal{L}_{DTW} + \lambda_{\text{multi}} \overbrace{\sum_e \alpha_e^{(i)} \sum (k_{\theta_e^{(i)}} - k_{\theta_{\text{best}}^{(i)}})^2}^{\mathcal{L}_{\text{multi}}}, \tag{5}$$

$$\text{with } k_{\theta_{\text{best}}^{(i)}} = \min_e \alpha_e^{(i)} \propto \sum (\mathbf{m}^{(i)} * k_{\theta_e^{(i)}} - \mathbf{d})^2 \tag{6}$$

Additionally, MSE loss for each EGF can be weighted with a user-defined parameter that can reflect the quality of each *a priori* selected EGF. Weights $\lambda_\phi, \lambda_2, \lambda_{DTW}$ and λ_{multi} were empirically chosen with a grid search on synthetic tests.

Section	Fig.	Tests	Suppl. Mat.	STF	# of EGFs	True EGF	Assumed EGF	Main event
3.1	1	a to s	S2, Figs S1-S4	Stack of $\boldsymbol{N_{STF} = 10}$ pulses with Gaussian shape, random weigths and widths	1	All arrivals, synthetic waveforms calculated with 1D crust, random source parameters, 10 Hz	All arrivals, source properties and crustal structure that randomly vary away from true EGF + white noise, PSNR 0 to 10 %	True EGF $*$ STF
		a0 to g4	S2, Figs S5-S10	$\boldsymbol{N_{STF} = 3}$	1	”	”	”
3.2			S3, Fig. S18	$\boldsymbol{N_{STF} = 3}$	1	All arrivals of recorded waveforms, 20 or 25 Hz	True EGF + noise, PSNR 3 % different for each component	True EGF $*$ STF + white noise, PSNR 3 %
	2		S3, Figs S19-S20	$\boldsymbol{N_{STF} = 10}$	1	P arrivals of recorded waveforms, 40 or 50 Hz	”	”
4.1	3		S4, Figs S21-33	$\boldsymbol{N_{STF} = 3}$	3	Randomly weighted sum of selected recorded EGFs + white noise PSNR 3 %, all arrivals, 20 Hz	Selected recorded EGFs, all arrivals	”
			S4, Figs S34-39	$\boldsymbol{N_{STF} = 10}$	4	Randomly weighted sum of selected recorded EGFs + white noise PSNR 3 %, P arrivals, 20 Hz	Selected recorded EGFs, P arrivals	”
	5		S4, Figs S38, S40	$\boldsymbol{N_{STF} = 10}$	8	”	”	”

Table 1. Summary of design choices for synthetic tests. Details are in Supplementary Material.

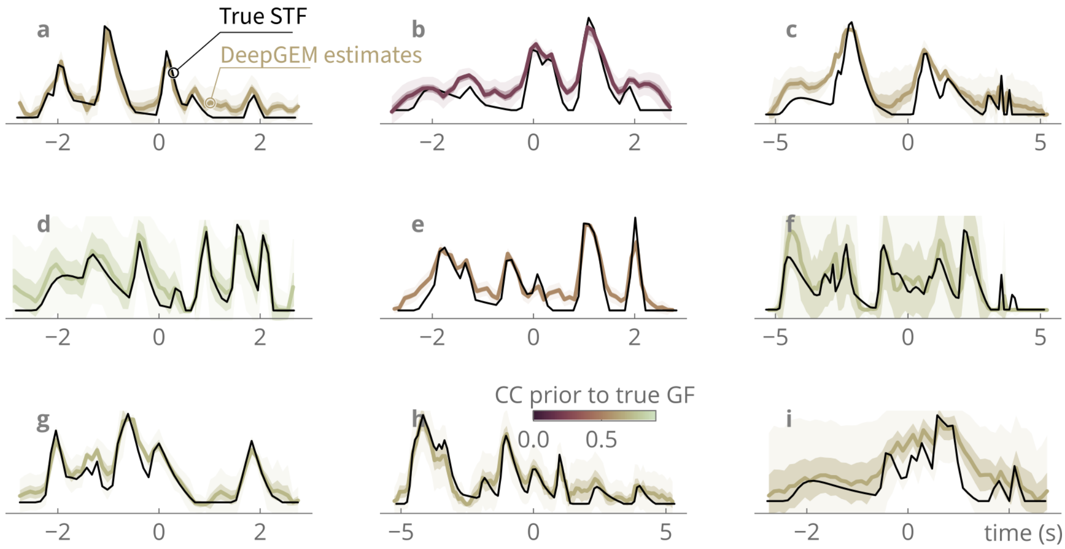

Figure 1. Inferred (colored) and target (black) Source-Time Functions (STFs) for toy models designed with fully synthetic waveforms. The mean of the STFs is colored by the peak cross-correlation value between prior and target Empirical Green's functions; the standard deviation is shaded (1σ darker, 3σ lighter).

3 Benchmark on toy models

We test the ability of DeepGEM-EGF to correctly infer STFs and EGFs on toy models, based on fully synthetic waveforms or recorded waveforms. A summary of those tests is presented in Table 3. For a few tests, we compare DeepGEM results with non-blind deconvolution approaches; a multitaper deconvolution approach (e.g., Thomson, 1982; Percival & Walden, 1993; Prieto et al., 2009) and an iterative Landweber approach (Bertero et al., 1997). We choose both these algorithms as they are well-documented and have been used extensively.

3.1 Tests with synthetic waveforms

We first perform two series of tests with fully synthetic waveforms calculated at 10 Hz, using all of the arrivals (P, S and coda). The target STF consists of a stack of 10 (tests a to n, Fig. 1, Suppl. Mat. Table S3) or 3 (tests listed in Suppl. Mat. Tables S4 and S5) pulses parameterized as Gaussian functions with randomly varying width and heights. Source parameters for the main event (the largest) are random. Source properties (location, depth, moment tensor) for synthetic EGFs randomly vary away from the properties of the main event. Kagan angle (Kagan, 1991) between moment tensors of the source and assumed EGFs vary between 5 and 40°. We add white noise, with a peak signal to noise ratio ranging from 0-10%, to waveforms of both the main event and EGFs. Full results are detailed in Suppl. Mat. section S2.

The results are promising: target STFs are well recovered, including multiple peaks of various frequencies (Fig. 1). The predicted waveforms fit the data well. The updated EGF waveforms are usually close to the target ones, even when the prior is off, without overfitting the additional noise. STF fits from a multitaper approach are outperformed, even for very simple tests (e.g., Suppl. Mat. Fig. S4). The choice of the prior EGF has a strong impact on the quality of the results: the larger the discrepancy between the assumed and target EGF waveforms, the larger the misfit between inferred and target STFs (see test b in Fig. 1). DeepGEM converges well even if the source of the prior EGF sees a time shift (changes in depth, location, velocity structure) or variations of up to ∼20° in Kagan angle (tests j to n, Suppl. Mat. Figs S1-S4).

Occasionally, our tests fail. These failures can be classified into two categories: either the forward model does not deviate sufficiently from the incorrect prior, or it becomes trapped in a local minimum. Good representatives of the first category are tests with Kagan angles exceeding 30° (tests o to s). In that case, most peaks of the STFs are correctly inferred, but the weight on the prior is too large for the EGF to fully update towards the correct solution. The second category occurs when the true forward model is too far from the prior, such as when the assumed velocity model significantly differs from the true one (e.g., tests 2b6 and 2g1 are accurate, but tests 2g* are inconclusive) or when initial EGFs are too noisy (added white noise PSNR reaches 10%, tests 2g7 and 2g8). In practice, such mismatch between prior and true forward models are rare due to the careful selection of EGFs.

3.2 Tests with recorded waveforms

We also perform a few synthetic tests using recorded waveforms as EGFs. We select, as EGFs, P arrivals of recordings in Southern California for an ML 3.37 event that occurred on 17 July 2014 near Borrego Springs, CA, USA (Figs. 2,3). To obtain waveforms for the main toy model event, we convolve those P arrivals to synthetic multi-peaked STFs (10 pulses, similarly to the previous toy models). We then decimate all waveforms to 40 Hz (for broadband) or 50 Hz (for accelerometers) to hasten the calculation process, and add white noise. These tests differ from the fully synthetic toy models mostly because of the duration of the data, which is close to the duration of the target STF, and the increased frequency content: the problem is much more underdetermined. Full results are detailed in Suppl. Mat., section S3.

The results of this experiment are overall consistent with those of the fully synthetic toy models. We recover most features of the target STFs in all frequency bands, with occasional misfit in amplitude, and a small tendency to overfit on noise at high frequencies. In general, target EGFs are well recovered. For stations BOR and TRO (Fig. 2h,i) we cannot gain information on a few model parameters, as expressed by the large posterior uncertainty on the boundaries of the inferred STF. This is probably because the duration of the P-arrivals is less than a third of the assumed STF duration, making the problem highly underdetermined. A larger weight on the boundary prior or a decreased frequency band could solve the issue; but we choose here to use similar hyperparameters for all the tests.

We also infer apparent STFs for each component with the Landweber approach (we visually select the best STF, orange in Fig. 2, more details in Suppl. Mat.). Baseline STFs are fair to poor, and only the first-order characteristics are retrieved: the frequency content is probably too high, and the problem too ill-posed for the method to perform correctly.

4 Case study: the 2016-2019 Cahuilla swarm, CA, USA

The Cahuilla swarm outlined a complex but well-defined fault structure between the San Jacinto and Elsinore fault zones (Fig. 5). Ross et al. (2020) produced a seismicity catalog of more than 22,000 events with Mw ranging from 0.7 to 4.4, all of those event seemingly affecting the same non-planar fault geometry. The main event (Mw 4.4) is ∼5 km deep and likely caused drastic changes in the evolution of the swarm by allowing fluids to circulate at shallower depth. We take advantage of this detailed seismic catalog, with many small events, to investigate how our forward model assumptions impacts our knowledge of the source. Along with evaluating the robustness of our approach and how

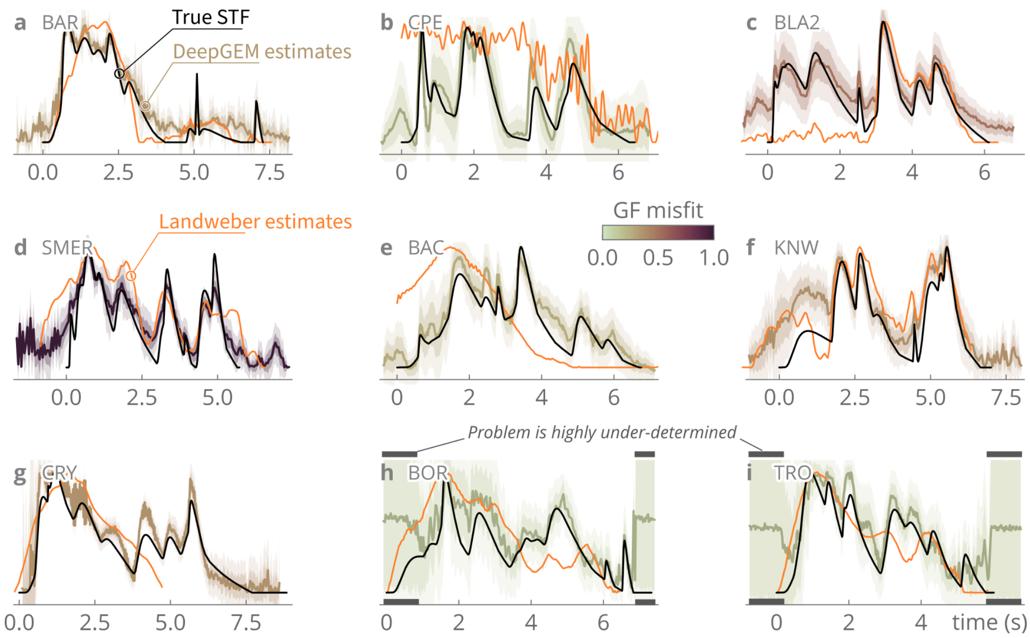

Figure 2. Inferred (colormap) and target (black) Source-Time Functions (STFs) for toy models designed with waveforms (P arrivals only) recorded for a M_L 3.37 event that occured in 2014 near Borrego Springs (CA). The mean of the STFs is colored from the normalized misfit between inferred and target Empirical Green's functions; the standard deviation is shaded (1σ darker, 3σ lighter). Apparent best fitting STFs calculated with the approach by Bertero et al. (1997) are shown in orange. Stations locations are shown in Figure 3. In (h) and (i), the problem is highly underdetermined and there is no information gained on the boundaries.

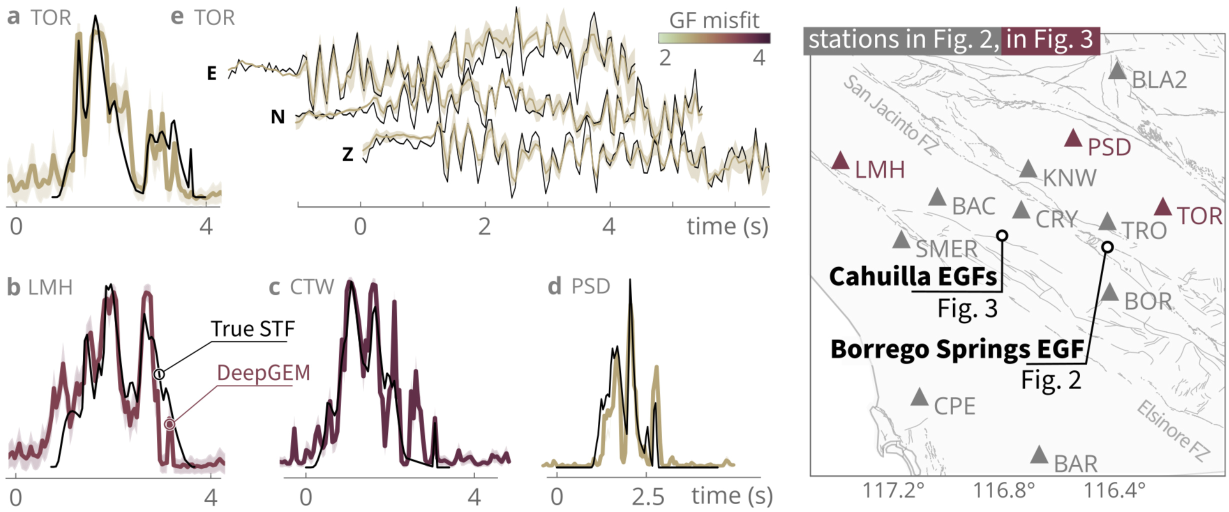

Figure 3. (a-d) Inferred (colored) and target (black) Source-Time Functions (STFs) for toy models designed with waveforms (P arrivals only) recorded for four neighbor M∼2 events that occurred during the Cahuilla swarm. The mean of the STFs is colored from the misfit between inferred and target Empirical Green's functions (EGFs); the standard deviation is shaded. (e) Best inferred (colored) and target (black) EGF for toy model (a). Stations locations are shown in the map on the right. CTW station is located to the north-west of TOR (see Fig. 5).

the ad-hoc selection of EGFs can affect the inferred source parameters, we aim to better characterize the source process of this puzzling event.

4.1 Toy models with multiple EGFs

We first design two sets of toy models that are different than the ones previously presented: we use several of the nearest Mw∼2 events to the mainshock as prior EGFs. The "true" EGF, or the one convolved with synthetic STFs to obtain mainshock waveforms, is defined as a randomly weighted sum of the *a priori* selected EGFs. We use two sets of prior EGFs. For one set, we use all arrivals for 3 EGF events (Figs. S21-33). For the other set, we use P arrivals for 4 EGF events (results in Figs. 3, S34-38). Note that as EGFs are selected based on distance and not semblance, their waveforms can differ significantly, making the example more difficult than with carefully selected waveforms. Full results are detailed in Suppl. Mat. section S4.2.

The misfit between the inferred and target STFs and EGFs is usually below 20% of the maximum amplitude for simple tests (Fig. S21), and increases with distance between prior and target EGFs. For more complex STFs, fit remains very good even if a few high frequency artifacts appear (Fig. 3). Target EGF events are generally close to the mean inferred EGFs and within posterior uncertainties (Figs. 3 and S22-38).

For station TOR, we also perform tests using four more EGFs (Figs. 4 and S38-40). In one case (Fig. 4c,d), the additional four waveforms are random linear combinations of the initial four prior EGFs: in other words, the additional waveforms do not contain more information than the initial four. In another case, the additional four waveforms are closer to the target EGF: they are equal to the target EGF to which 10% of the random linear combination is added (Fig. 4e,f). As expected, if additional EGFs do not add information content, the inferred model is not improved. By contrast, adding informative EGFs (i.e. more accurate EGFs) improves the quality of the inferred STF. Adding information only

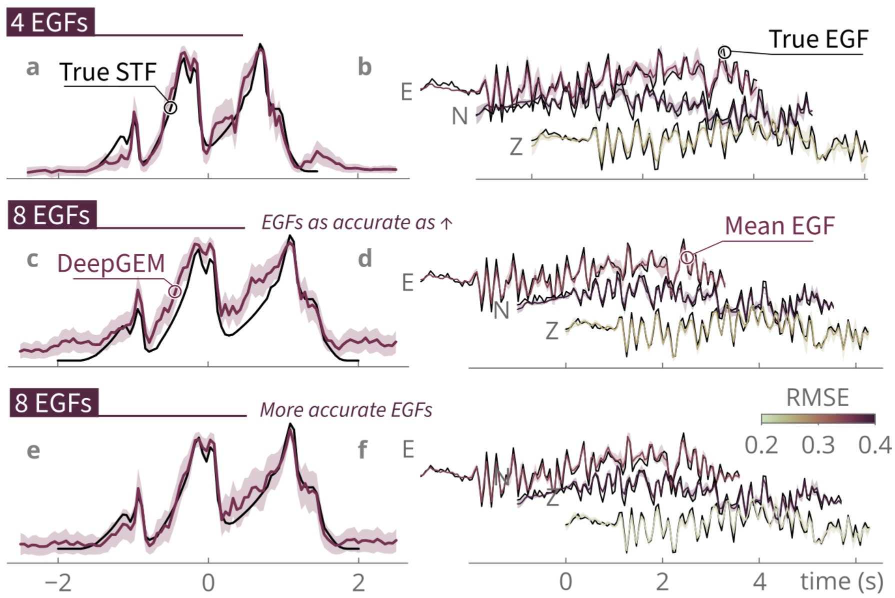

Figure 4. Mean inferred (colored) and target (black) Source-Time Functions (STFs) and Empirical Green's Functions for toy models designed with waveforms (P arrivals only) recorded for four (a,b) or eight (c-f) neighboring M$\sim$2 events that occurred during the Cahuilla swarm. In (e,f) the additional four waveforms are closer to the target than in (c,d). Standard deviation (1σ) is shaded. EGFs are colored by the root mean squared error (RMSE) between data and average predictions normalized for each component.

very slightly improves the fit to the data. It is therefore more efficient to assume a few well selected prior EGFs than multiple poorly constrained priors. These tests further confirm the robustness of DeepGEM-EGF, and its capacity to use good information.

4.2 Results

We compare the STFs inferred, at stations within 100 km of the mainshock, assuming three different sets of prior EGFs decimated to 20 Hz: 1. minimizing distance (set A, Fig 5a); 2. minimizing cross-correlation at one station (set B, Fig 5b); 3. minimizing cross-correlation (set C, Fig 5c,d) between EGFs and the mainshock. In set B, selected EGFs are less than 1 km away from the mainshock and maximize the cross-correlation with the mainshock waveforms at station PLM. This choice of station is based on the quality of the waveforms and the deconvolution with set A (Fig. S57). For set C, prior EGFs are selected based on their cross-correlation with the mainshock waveforms at each station, are less than 1 km away from the mainshock, and their number vary between 1 and 4 depending on their SNR. We use either P waves arrivals (Fig 5a-c) or S waves arrivals (for set C only, Fig 5d), and assume similar priors and hyperparameters. We expect the STFs inferred with set C to be our best estimates; and the ones estimated with set B to be the worst, as EGFs are incorrectly constrained with a single station. Full results are detailed in Suppl. Mat. sections S4.3 and S4.4.

For all sets of EGFs, inferred STFs share similar first-order characteristics: width, shape and azimuthal variations. As expected, STFs estimated with set B, while consistent between neighbor stations, show many high frequency peaks, which indicate their relatively poor quality compared to results with other sets (Figs S42, S46, S50, S54 for

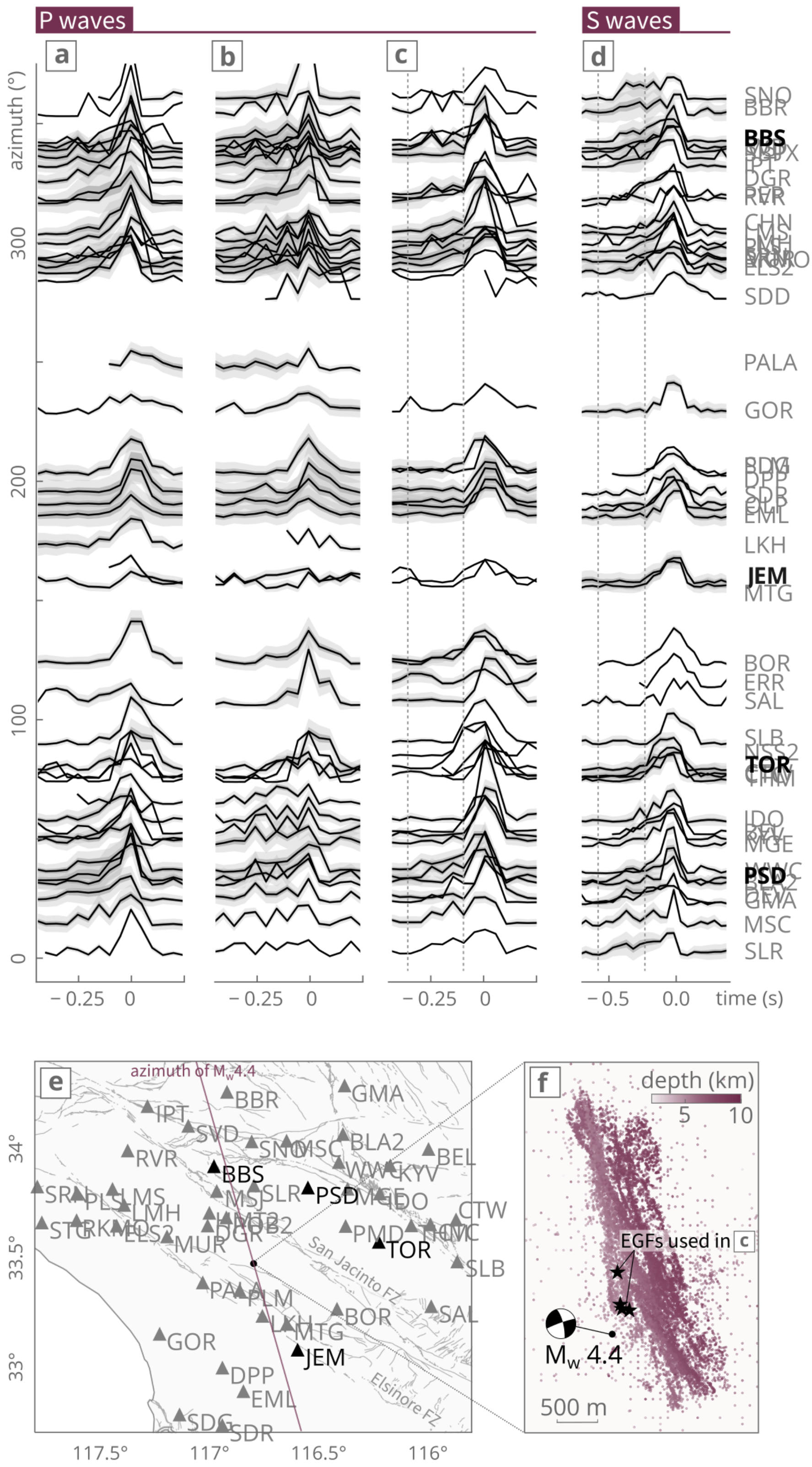

Figure 5. Impact of the choice of candidate EGFs on the apparent STFs of the 2018 Mw 4.41 mainshock that occurred during the Cahuilla swarm. (e) Stations locations and (f) relocated catalog for the swarm and EGFs used. (a-d) STFs inferred assuming up to 4 M∼2 event as prior EGFs. The posterior mean is in black, the posterior σ in gray. We assume as prior EGFs: (a) 4 events nearest to the mainshock, (b) 4 events maximizing EGF/mainshock waveform cross-correlation at station PLM, (c) and (d) up to 4 events maximizing EGF/mainshock waveform cross-correlation at each station. We use P wave arrivals in (a) to (c), and S wave arrivals in (d). STFs are aligned on their peak value: if the peak is off or shifted, the STF appears as partial.

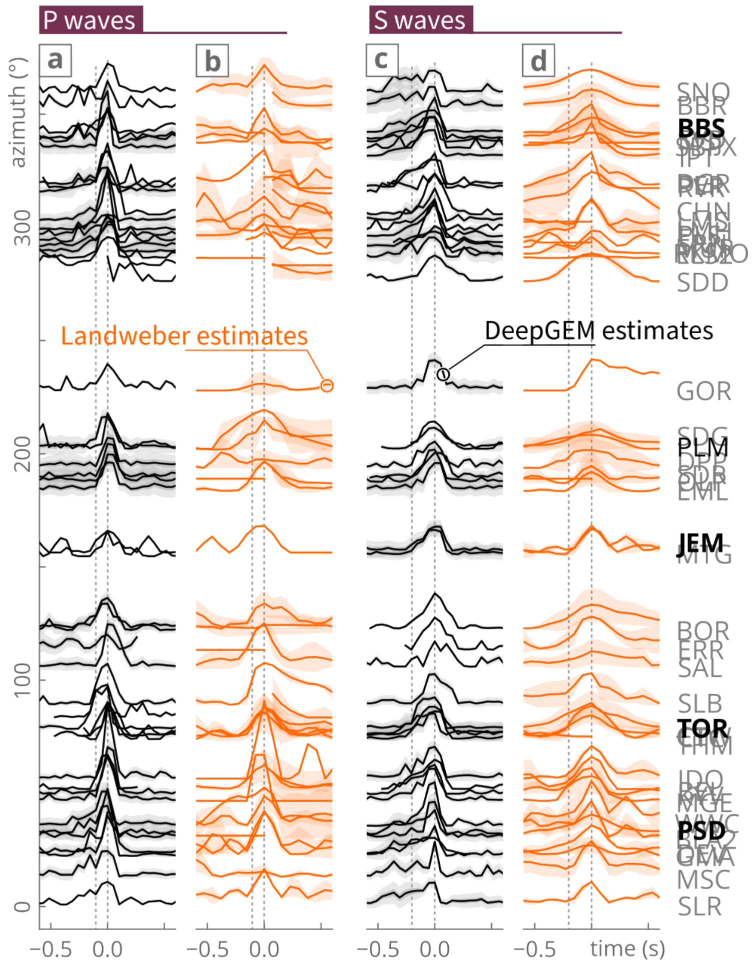

Figure 6. STFs inferred for the 2018 Mw 4.41 mainshock of the Cahuilla swarm assuming the same prior EGFs as in Fig 5, using DeepGEM-EGF (mean in black) or with the approach of Bertero et al. (1997, mean for several components and EGFs in orange, standard deviation σ shaded). Note that σ estimates for the Landweber approach derive from the variability of multiples EGFs and their components, and not from posterior PDFs as for DeepGEM results. (left) Using P arrivals only (similar to Fig. 5e) or (right) using S arrivals only (same as Fig. 5f).

stations BOR, BLA2, PLS and LMH, respectively). Small posterior uncertainty on both STFs and EGFs might suggest that over-constraining EGFs to an incorrect prior induced the model to fall into a local minimum. In contrast, STFs estimated with sets A and C are smoother and more similar, and furthermore have increased posterior uncertainty and overall improved fit (particulary with set C, see Figs S41 to S60). For this latter set, STFs shapes are more coherent across stations, for instance with two small pulses preceding the largest peak around station BBS (Fig. 5e). In particular, using S arrivals, we infer similar apparent STFs at two close stations (JEM and MTG or PSD and WWC), confirming the robustness of our approach.

We finally compare our preferred STFs (set C) to apparent STFs estimated with a widely used frequency-domain deconvolution approach (or Landweber approach, from Bertero et al., 1997). With this latter method, we derive means and standard deviations from estimates of apparent STFs for each component of each prior EGF (Fig 6). The Landweber STFs are smooth, often largely over-estimate the STF duration (in particular for S arrivals), and show a large posterior uncertainty. P-wave pulse-like STFs are relatively well-imaged around station PSD but not to the north of the swarm, and apparent STFs for both methods are of similar shape for a few stations only (JEM, TOR, SAL). Even for those stations, STFs derived from the baseline approach are less informative: for instance, S-arrivals apparent STFs at station JEM (Fig. 6c,d) are symmetric, or by contrast clearly asymmetric, when estimated with the Landweber or DeepGEM approach, respectively.

Results from both methods indicate that apparent STFs are narrower for stations located NE of the Cahuilla swarm. Our deconvolution approach allows us to reach a greater level of detail: for stations to the north of the swarm (BBS, PSD), apparent STFs are complex and long in duration, with two small peaks preceding an energetic pulse, especially around stations PSD and MGE. To the South (stations SDD to TOR), apparent STFs are wider and more Gaussian-like. The pulse-like shape of STFs around stations PSD and IDO suggests a down-dip directivity of the Mw 4.4 event towards the northern portion of the fault. Narrow STFs around station BBS might also suggest along-strike directivity towards the north.

5 Discussion and conclusions

We introduce DeepGEM-EGF, a Bayesian joint inversion method for improving the source deconvolution problem. We show through tests on toy models, synthetic tests with real waveforms, and a case study in California, that this approach effectively discriminates source parameters given approximations made in the forward model. Specifically, DeepGEM-EGF robustly estimates complex apparent STFs with high-frequency content ($>$40 Hz) and exhibits limited sensitivity to prior EGF selection. Additionally, DeepGEM-EGF estimates posterior uncertainties for both STFs and EGFs (where multiple priors are assumed), ensuring our ability to track the impact of epistemic uncertainty on source estimates.

DeepGEM-EGF explicitly accounts for epistemic uncertainties and provides probabilistic estimates of source parameters in the time domain, advancing beyond deterministic and frequency-domain methods. Compared to these traditional deconvolution techniques, DeepGEM-EGF provides more robust, coherent, and informative results, which remain stable for various choices of prior EGFs. The proposed approach may underperform for highly underdetermined scenarios, or when prior EGFs deviate significantly from the true solution, i.e. when the EGF assumption does not hold anymore.

Understanding earthquake self-similarity across scales is crucial for advancing physical models and improving hazard assessments. Self-similarity is often explored using two key proxies: source complexity and stress drop. Both stress drop (Atkinson & Beresnev, 1997; Abercrombie, 2021; Bindi et al., 2023; A. Baltay et al., 2024; Neely et al., 2024) and metrics of source complexity (Vallée & Douet, 2016; Danré et al., 2019; Pennington et al., 2023; Neely et al., 2024) are uncertain and variable, and even more difficult to constrain for smaller magnitude events due to increased noise and frequency content and the scarcity of observations. DeepGEM-EGF can address these challenges by reliably imaging complex, multi-peaked STFs under noisy conditions, while staying methodologically consistent across magnitudes (e.g., Neely et al., 2024; A. Baltay et al., 2024). We aim for this joint approach to become a valuable tool for disentangling the variability of the seismic source, and stress drop, from artifacts introduced by modeling assumptions. DeepGEM-EGF is available as an open-source tool.

Code and data availability

DeepGEM-EGF is available at `https://github.com/thearagon/DeepGEM_EGF` and stored at `https://doi.org/10.5281/zenodo.14472786`. A running example is available on the same repository. We used waveform data recorded by the regional (CI, California Institute of Technology and United States Geological Survey Pasadena, 1926), ANZA (AZ, Frank Vernon, 1982) and UCSB (SB, UC Santa Barbara, 1989) networks in Southern California.

Acknowledgements

We thank Mathieu Causse and Emile Denise for fruitful discussions. ZR is supported by the David and Lucile Packard Foundation and the US National Science Foundation.

References

Abercrombie, R. E. (2015). Investigating uncertainties in empirical Green's function analysis of earthquake source parameters. *Journal of Geophysical Research: Solid Earth*, *120*(6), 4263–4277. doi: 10.1002/2015JB011984

Abercrombie, R. E. (2021). Resolution and uncertainties in estimates of earthquake stress drop and energy release. *Philosophical Transactions of the Royal Society A: Mathematical, Physical and Engineering Sciences*, *379*(2196), 20200131. doi: 10.1098/rsta.2020.0131

Abercrombie, R. E., Poli, P., & Bannister, S. (2017). Earthquake Directivity, Orientation, and Stress Drop Within the Subducting Plate at the Hikurangi Margin, New Zealand. *Journal of Geophysical Research: Solid Earth*, *122*(12), 10,176–10,188. doi: 10.1002/2017JB014935

Abercrombie, R. E., & Rice, J. R. (2005). Can observations of earthquake scaling constrain slip weakening? *Geophysical Journal International*, *162*(2), 406–424. doi: 10.1111/j.1365-246X.2005.02579.x

Aki, K. (1967). Scaling law of seismic spectrum. *Journal of Geophysical Research (1896-1977)*, *72*(4), 1217–1231. doi: 10.1029/JZ072i004p01217

Aki, K. (1996). Scale dependence in earthquake phenomena and its relevance to earthquake prediction. *Proceedings of the National Academy of Sciences*, *93*(9), 3740–3747. doi: 10.1073/pnas.93.9.3740

Anderson, J. G., & Brune, J. N. (1999). Probabilistic Seismic Hazard Analysis without the Ergodic Assumption. *Seismological Research Letters*, *70*(1), 19–28. doi: 10.1785/gssrl.70.1.19

Andrews, D. J. (1986). Objective Determination of Source Parameters and Similarity of Earthquakes of Different Size. In *Earthquake Source Mechanics* (pp. 259–267). American Geophysical Union (AGU). doi: 10.1029/GM037p0259

Atkinson, G. M., & Beresnev, I. (1997). Don't Call it Stress Drop. *Seismological Research Letters*, *68*(1), 3–4. doi: 10.1785/gssrl.68.1.3

Baltay, A., Abercrombie, R., Chu, S., & Taira, T. (2024). The SCEC/USGS Community Stress Drop Validation Study Using the 2019 Ridgecrest Earthquake Sequence. *Seismica*, *3*(1). doi: 10.26443/seismica.v3i1.1009

Baltay, A. S., Hanks, T. C., & Beroza, G. C. (2013). Stable Stress-Drop Measurements and their Variability: Implications for Ground-Motion Prediction. *Bulletin of the Seismological Society of America*, *103*(1), 211–222. doi: 10.1785/0120120161

Bell-Kligler, S., Shocher, A., & Irani, M. (2019). Blind Super-Resolution Kernel Estimation using an Internal-GAN. *arXiv e-prints*, arXiv:1909.06581. doi: 10.48550/arXiv.1909.06581

Bertero, M., Bindi, D., Boccacci, P., Cattaneo, M., Eva, C., & Lanza, V. (1997). Application of the projected Landweber method to the estimation of the source time function in seismology. *Inverse Problems*, *13*(2), 465. doi: 10.1088/0266-5611/13/2/017

Bindi, D., Pacor, F., Luzi, L., Massa, M., & Ameri, G. (2009). The Mw 6.3, 2009 L'Aquila earthquake: Source, path and site effects from spectral analysis of strong motion data. *Geophysical Journal International*, *179*(3), 1573–1579. doi: 10.1111/j.1365-246X.2009.04392.x

Bindi, D., Spallarossa, D., Picozzi, M., Oth, A., Morasca, P., & Mayeda, K. (2023). The Community Stress-Drop Validation Study—Part I: Source, Propagation, and Site Decomposition of Fourier Spectra. *Seismological Research Letters*, *94*(4), 1980–1991. doi: 10.1785/0220230019

Boatwright, J. (1984). The effect of rupture complexity on estimates of source size. *Journal of Geophysical Research: Solid Earth*, *89*(B2), 1132–1146. doi: 10.1029/JB089iB02p01132

Boore, D. M. (2003). Simulation of Ground Motion Using the Stochastic Method. In Y. Ben-Zion (Ed.), *Seismic Motion, Lithospheric Structures, Earthquake and Volcanic Sources: The Keiiti Aki Volume* (pp. 635–676). Basel: Birkhäuser. doi: 10.1007/978-3-0348-8010-7_10

California Institute of Technology and United States Geological Survey Pasadena. (1926). *Southern california seismic network.* International Federation of Digital Seismograph Networks. doi: 10.7914/SN/CI

Cocco, M., Tinti, E., & Cirella, A. (2016). On the scale dependence of earthquake stress drop. *Journal of Seismology*, *20*(4), 1151–1170. doi: 10.1007/s10950-016-9594-4

Cotton, F., Archuleta, R., & Causse, M. (2013). What is Sigma of the Stress Drop? *Seismological Research Letters*, *84*(1), 42–48. doi: 10.1785/0220120087

Courboulex, F., Vallée, M., Causse, M., & Chounet, A. (2016). Stress-Drop Variability of Shallow Earthquakes Extracted from a Global Database of Source Time Functions. *Seismological Research Letters*, *87*(4), 912–918. doi: 10.1785/0220150283

Courboulex, F., Virieux, J., Deschamps, A., Gibert, D., & Zollo, A. (1996). Source investigation of a small event using empirical Green's functions and simulated annealing. *Geophysical Journal International*, *125*(3), 768–780. doi: 10.1111/j.1365-246X.1996.tb06022.x

Danré, P., Yin, J., Lipovsky, B. P., & Denolle, M. A. (2019). Earthquakes Within Earthquakes: Patterns in Rupture Complexity. *Geophysical Research Letters*, *46*(13), 7352–7360. doi: 10.1029/2019GL083093

Dinh, L., Sohl-Dickstein, J., & Bengio, S. (2016). *Density estimation using Real NVP.* https://arxiv.org/abs/1605.08803v3.

Dreger, D. S. (1994). Empirical Green's function study of the January 17, 1994 Northridge, California earthquake. *Geophysical Research Letters*, *21*(24), 2633–2636. doi: 10.1029/94GL02661

Frank Vernon. (1982). *ANZA regional network.* International Federation of Digital Seismograph Networks. doi: 10.7914/SN/AZ

Frankel, A., Fletcher, J., Vernon, F., Haar, L., Berger, J., Hanks, T., & Brune, J. (1986). Rupture characteristics and tomographic source imaging of ML ~ 3 earthquakes near Anza, southern California. *Journal of Geophysical Research: Solid Earth*, *91*(B12), 12633–12650. doi: 10.1029/JB091iB12p12633

Frankel, A., & Kanamori, H. (1983). Determination of rupture duration and stress drop for earthquakes in southern California. *Bulletin of the Seismological Society of America*, *73*(6A), 1527–1551. doi: 10.1785/BSSA07306A1527

Gallegos, A., & Xie, J. (2020). A multichannel deconvolution method to retrieve source–time functions: Application to the regional Lg wave. *Geophysical Journal International*, *223*(1), 323–347. doi: 10.1093/gji/ggaa303

Gao, A. F., Castellanos, J. C., Yue, Y., Ross, Z. E., & Bouman, K. (2021). DeepGEM: Generalized Expectation-Maximization for Blind Inversion. In *Thirty-Fifth Conference on Neural Information Processing Systems.*

Garcia-Aristizabal, A., Caciagli, M., & Selva, J. (2016). Considering uncertainties in the determination of earthquake source parameters from seismic spectra. *Geophysical Journal International*, *207*(2), 691–701. doi: 10.1093/gji/ggw303

Gerstenberger, M. C., Marzocchi, W., Allen, T., Pagani, M., Adams, J., Danciu, L., … Petersen, M. D. (2020). Probabilistic Seismic Hazard Analysis at Regional and National Scales: State of the Art and Future Challenges. *Reviews of Geophysics*, *58*(2), e2019RG000653. doi: 10.1029/2019RG000653

Godano, M., Bernard, P., & Dublanchet, P. (2015). Bayesian inversion of seismic spectral ratio for source scaling: Application to a persistent multiplet in the western Corinth rift. *Journal of Geophysical Research: Solid Earth*, *120*(11), 7683–7712. doi: 10.1002/2015JB012217

Hardebeck, J. L. (2020). Are the Stress Drops of Small Earthquakes Good Predictors of the Stress Drops of Moderate-to-Large Earthquakes? *Journal of Geophysical Research: Solid Earth*, *125*(3), e2019JB018831. doi: 10.1029/2019JB018831

Hartzell, S. H. (1978). Earthquake aftershocks as Green's functions. *Geophysical Research Letters*, *5*(1), 1–4. doi: 10.1029/GL005i001p00001

Hough, S. E. (1997a). Empirical Green's function analysis: Taking the next step. *Journal of Geophysical Research: Solid Earth*, *102*(B3), 5369–5384. doi: 10.1029/96JB03488

Hough, S. E. (1997b). Empirical Green's function analysis: Taking the next step. *Journal of Geophysical Research: Solid Earth*, *102*(B3), 5369–5384. doi: 10.1029/96JB03488

Hutchings, L., & Wu, F. (1990). Empirical Green's Functions from small earthquakes: A waveform study of locally recorded aftershocks of the 1971 San Fernando Earthquake. *Journal of Geophysical Research: Solid Earth*, *95*(B2), 1187–1214. doi: 10.1029/JB095iB02p01187

Ihmlé, P. F. (1996). Monte Carlo slip inversion in the frequency domain Application to the 1992 Nicaragua Slow Earthquake. *Geophysical Research Letters*, *23*(9), 913–916. doi: 10.1029/96GL00872

Kagan, Y. Y. (1991). 3-D rotation of double-couple earthquake sources. *Geophysical Journal International*, *106*(3), 709–716. doi: 10.1111/j.1365-246X.1991.tb06343.x

Kanamori, H., & Brodsky, E. E. (2004). The physics of earthquakes. *Reports on Progress in Physics*, *67*(8), 1429. doi: 10.1088/0034-4885/67/8/R03

Kane, D. L., Kilb, D. L., & Vernon, F. L. (2013). Selecting Empirical Green's Functions in Regions of Fault Complexity: A Study of Data from the San Jacinto Fault Zone, Southern California. *Bulletin of the Seismological Society of America*, *103*(2A), 641–650. doi: 10.1785/0120120189

Kane, D. L., Prieto, G. A., Vernon, F. L., & Shearer, P. M. (2011). Quantifying Seismic Source Parameter Uncertainties. *Bulletin of the Seismological Society of America*, *101*(2), 535–543. doi: 10.1785/0120100166

Kingma, D. P., & Ba, J. (2014). Adam: A Method for Stochastic Optimization. In *3rd International Conference for Learning Representations.* San Diego.

Lambert, V., Lapusta, N., & Faulkner, D. (2021). Scale Dependence of Earthquake Rupture Prestress in Models With Enhanced Weakening: Implications for Event Statistics and Inferences of Fault Stress. *Journal of Geophysical Research: Solid Earth*, *126*(10), e2021JB021886. doi: 10.1029/2021JB021886

Lin, Y.-Y., & Lapusta, N. (2018). Microseismicity Simulated on Asperity-Like Fault Patches: On Scaling of Seismic Moment With Duration and Seismological Estimates of Stress Drops. *Geophysical Research Letters*, *45*(16), 8145–8155. doi: 10.1029/2018GL078650

McGuire, J. J. (2004). Estimating Finite Source Properties of Small Earthquake Ruptures. *Bulletin of the Seismological Society of America*, *94*(2), 377–393. doi: 10.1785/0120030091

Mueller, C. S. (1985). Source pulse enhancement by deconvolution of an empirical Green's function. *Geophysical Research Letters*, *12*(1), 33–36. doi: 10.1029/GL012i001p00033

Neely, J. S., Park, S., & Baltay, A. (2024). The Impact of Source Time Function Complexity on Stress-Drop Estimates. *Bulletin of the Seismological Society of America*. doi: 10.1785/0120240022

Oth, A., Miyake, H., & Bindi, D. (2017). On the relation of earthquake stress drop and ground motion variability. *Journal of Geophysical Research: Solid Earth*, *122*(7), 5474–5492. doi: 10.1002/2017JB014026

Pavic, R., Koller, M. G., Bard, P.-Y., & Lacave-Lachet, C. (2000). Ground motion prediction with the empirical Green's function technique: An assessment of uncertainties and confidence level. *Journal of Seismology*, *4*(1), 59–77. doi: 10.1023/A:1009826529269

Pennington, C. N., Wu, Q., Chen, X., & Abercrombie, R. E. (2023). Quantifying rupture characteristics of microearthquakes in the Parkfield Area using a high-resolution borehole network. *Geophysical Journal International*, *233*(3), 1772–1785. doi: 10.1093/gji/ggad023

Percival, D. B., & Walden, A. T. (1993). Spectral Analysis for Physical Applications. *Spectral Analysis for Physical Applications.*

Plourde, A. P., & Bostock, M. G. (2017). Multichannel Deconvolution for Earthquake Apparent Source Time Functions. *Bulletin of the Seismological Society of America*, *107*(4), 1904–1913. doi: 10.1785/0120170015

Prieto, G. A., Parker, R. L., Vernon, F. L., Shearer, P. M., & Thomson, D. J. (2006). Uncertainties in Earthquake Source Spectrum Estimation Using Empirical Green Functions. In *Earthquakes: Radiated Energy and the Physics of Faulting* (pp. 69–74). American Geophysical Union (AGU). doi: 10.1029/170GM08

Prieto, G. A., Parker, R. L., & Vernon III, F. L. (2009). A Fortran 90 library for multitaper spectrum analysis. *Computers & Geosciences*, *35*(8), 1701–1710. doi: 10.1016/j.cageo.2008.06.007

Ross, Z. E., Cochran, E. S., Trugman, D. T., & Smith, J. D. (2020). 3D fault architecture controls the dynamism of earthquake swarms. *Science*, *368*(6497), 1357–1361. doi: 10.1126/science.abb0779

Shearer, P. M., Abercrombie, R. E., Trugman, D. T., & Wang, W. (2019). Comparing EGF Methods for Estimating Corner Frequency and Stress Drop From P Wave Spectra. *Journal of Geophysical Research: Solid Earth*, *124*(4), 3966–3986. doi: 10.1029/2018JB016957

Shearer, P. M., Prieto, G. A., & Hauksson, E. (2006). Comprehensive analysis of earthquake source spectra in southern California. *Journal of Geophysical Research: Solid Earth*, *111*(B6). doi: 10.1029/2005JB003979

Sun, H., & Bouman, K. L. (2021). Deep Probabilistic Imaging: Uncertainty Quantification and Multi-modal Solution Characterization for Computational Imaging. In *The Astrophysical Journal.* doi: 10.48550/arXiv.2010.14462

Sun, H., Bouman, K. L., Tiede, P., Wang, J. J., Blunt, S., & Mawet, D. (2022). α-deep Probabilistic Inference (α-DPI): Efficient Uncertainty Quantification from Exoplanet Astrometry to Black Hole Feature Extraction. *The Astrophysical Journal*, *932*(2), 99. doi: 10.3847/1538-4357/ac6be9

Supino, M., Festa, G., & Zollo, A. (2019). A probabilistic method for the estimation of earthquake source parameters from spectral inversion: Application to the 2016–2017 Central Italy seismic sequence. *Geophysical Journal International*, *218*(2), 988–1007. doi: 10.1093/gji/ggz206

Thomson, D. (1982). Spectrum estimation and harmonic analysis. *Proceedings of the IEEE*, *70*(9), 1055–1096. doi: 10.1109/PROC.1982.12433

Törnman, W., Martinsson, J., & Dineva, S. (2021). Robust Bayesian estimator for S-wave spectra, using a combined empirical Green's function. *Geophysical Journal International*, *227*(1), 403–438. doi: 10.1093/gji/ggab184

Trugman, D. T. (2022). Resolving Differences in the Rupture Properties of M5 Earthquakes in California Using Bayesian Source Spectral Analysis. *Journal* *of Geophysical Research: Solid Earth*, *127*(4), e2021JB023526. doi: 10.1029/2021JB023526

Trugman, D. T., & Shearer, P. M. (2017). Application of an improved spectral decomposition method to examine earthquake source scaling in Southern California. *Journal of Geophysical Research: Solid Earth*, *122*(4), 2890–2910. doi: 10.1002/2017JB013971

UC Santa Barbara. (1989). *UC santa barbara engineering seismology network.* International Federation of Digital Seismograph Networks. doi: 10.7914/SN/SB

Vallée, M. (2004). Stabilizing the Empirical Green Function Analysis: Development of the Projected Landweber Method. *Bulletin of the Seismological Society of America*, *94*(2), 394–409. doi: 10.1785/0120030017

Vallée, M., & Douet, V. (2016). A new database of source time functions (STFs) extracted from the SCARDEC method. *Physics of the Earth and Planetary Interiors*, *257*, 149–157. doi: 10.1016/j.pepi.2016.05.012

Van Houtte, C., & Denolle, M. (2018). Improved Model Fitting for the Empirical Green's Function Approach Using Hierarchical Models. *Journal of Geophysical Research: Solid Earth*, *123*(4), 2923–2942. doi: 10.1002/2017JB014943

Viegas, G., Abercrombie, R. E., & Kim, W.-Y. (2010). The 2002 M5 Au Sable Forks, NY, earthquake sequence: Source scaling relationships and energy budget. *Journal of Geophysical Research: Solid Earth*, *115*(B7). doi: 10.1029/2009JB006799

Viesca, R. C., & Garagash, D. I. (2015). Ubiquitous weakening of faults due to thermal pressurization. *Nature Geoscience*, *8*(11), 875–879. doi: 10.1038/ngeo2554

Zollo, A., Capuano, P., & Singh, S. K. (1995). Use of small earthquake records to determine the source time functions of larger earthquakes: An alternative method and an application. *Bulletin of the Seismological Society of America*, *85*(4), 1249–1256. doi: 10.1785/BSSA0850041249